Ocean Modelling 157 (2021) 101722

Contents lists available at ScienceDirect

Ocean Modelling

journal homepage: www.elsevier.com/locate/ocemod

The impact of vertical resolution in reducing biases in sea surface temperature in a tropical Pacific Ocean model

Yanli Jia [a,*], Kelvin J. Richards [a,b], H. Annamalai [a,b]

[a] International Pacific Research Center, University of Hawai'i at Mānoa, Honolulu, HI, USA
[b] Department of Oceanography, University of Hawai'i at Mānoa, Honolulu, HI, USA

ARTICLE INFO

Keywords:
Sea surface temperature
Fine scale velocity shear
Stratification
Vertical mixing
Pycnocline
Kelvin waves

ABSTRACT

Motivated by observations of fine scale vertical shear and its contribution to mixing in the tropical ocean, this study explores the impact of vertical resolution in an ocean model on sea surface temperature in the tropical Pacific Ocean. We conduct two model experiments that differ in the vertical discretization only, with the grid spacing in one being significantly smaller than the other in the upper ocean. We examine the temperature difference between the high and low vertical resolution experiments. We find that the difference in the uppermost layer is positive in the equatorial cold tongue and negative along the South American coast, thus reducing the commonly seen cool and warm biases in the two regions, respectively. The change in the structure of the vertical diffusivity, as determined by the K-profile parameterization, is identified as the primary cause in reducing the biases. In the central equatorial Pacific, the change in the vertical diffusivity from low to high vertical resolution in the upper pycnocline results in a positive temperature difference that propagates eastward as an equatorial Kelvin wave, rising to the sea surface in the central and eastern regions to increase the sea surface temperature there. In the far eastern equatorial Pacific, the change in the vertical diffusivity in the lower pycnocline produces a negative temperature difference that propagates poleward as coastal Kelvin waves along the west coast of the American continent, outcropping along the South American coast to reduce the sea surface temperature there. The high vertical resolution experiment captures much of the small-scale vertical velocity shear and resolves the fine details of the stratification in the upper ocean. Our analysis suggests that the shear-generated turbulence is the primary contributor to the change in the vertical diffusivity in the central region whereas stratification is the dominant factor in the far eastern region.

1. Introduction

Sea surface temperature (SST), the principal communicator of the ocean with the atmosphere, plays a very important role in the tropical Pacific. Yet, many ocean models and coupled atmosphere-ocean models often have difficulties in correctly reproducing its observed characteristics. The cool bias of the cold tongue in the eastern equatorial Pacific and the warm bias off the South American coast are two such examples.

The cool bias of the cold tongue is generally associated with too intense easterly trade winds in the western and central Pacific. It is difficult to determine the root cause of this bias because of the complex feedback mechanisms of the atmosphere-ocean system, but there have been many studies that try. For example, Vannière et al. (2014) investigated SST biases in the tropical Pacific with a multitude of simulations using ocean-only, atmosphere-only and coupled atmosphere-ocean models. They suggested that a cool bias in the subtropical regions could give rise to a cool bias in the equatorial cold tongue transmitted through advection by the subtropical cells (STCs, McCreary and Lu, 1994) and propagation by ocean waves. This mechanism is supported by the analysis of Burls et al. (2017) using output from climate models that participate in the Coupled Model Intercomparison Project Phase 5 (CMIP5). They found a high correlation in SST between the equatorial zone and the extra-tropical subduction regions across the CMIP5 models, and a link between positive cloud albedo bias (thus reduced shortwave radiation into the ocean) and negative SST bias in extra-tropical regions. Li and Xie (2012, 2014), by comparing CMIP5 and CMIP3 models with their corresponding atmosphere-only models, came to a similar conclusion that a high cloud coverage in the atmospheric models is correlated to a cool bias in the mean SST across all tropical oceans. Additionally, Li and Xie (2012, 2014) suggested that a shallow thermocline in the upwelling region of the equatorial Pacific in the ocean components of the coupled models is the cause of a cool bias in the cold tongue, and through the Bjerknes (1969) feedback mechanism, a positive bias in the easterly winds arises as a result. The basis for this conclusion is that the wind bias does not exist in atmosphere-only models forced with observed SST.

* Corresponding author.
E-mail address: yjia@hawaii.edu (Y. Jia).

https://doi.org/10.1016/j.ocemod.2020.101722
Received 4 May 2020; Received in revised form 15 October 2020; Accepted 1 November 2020
Available online 9 November 2020

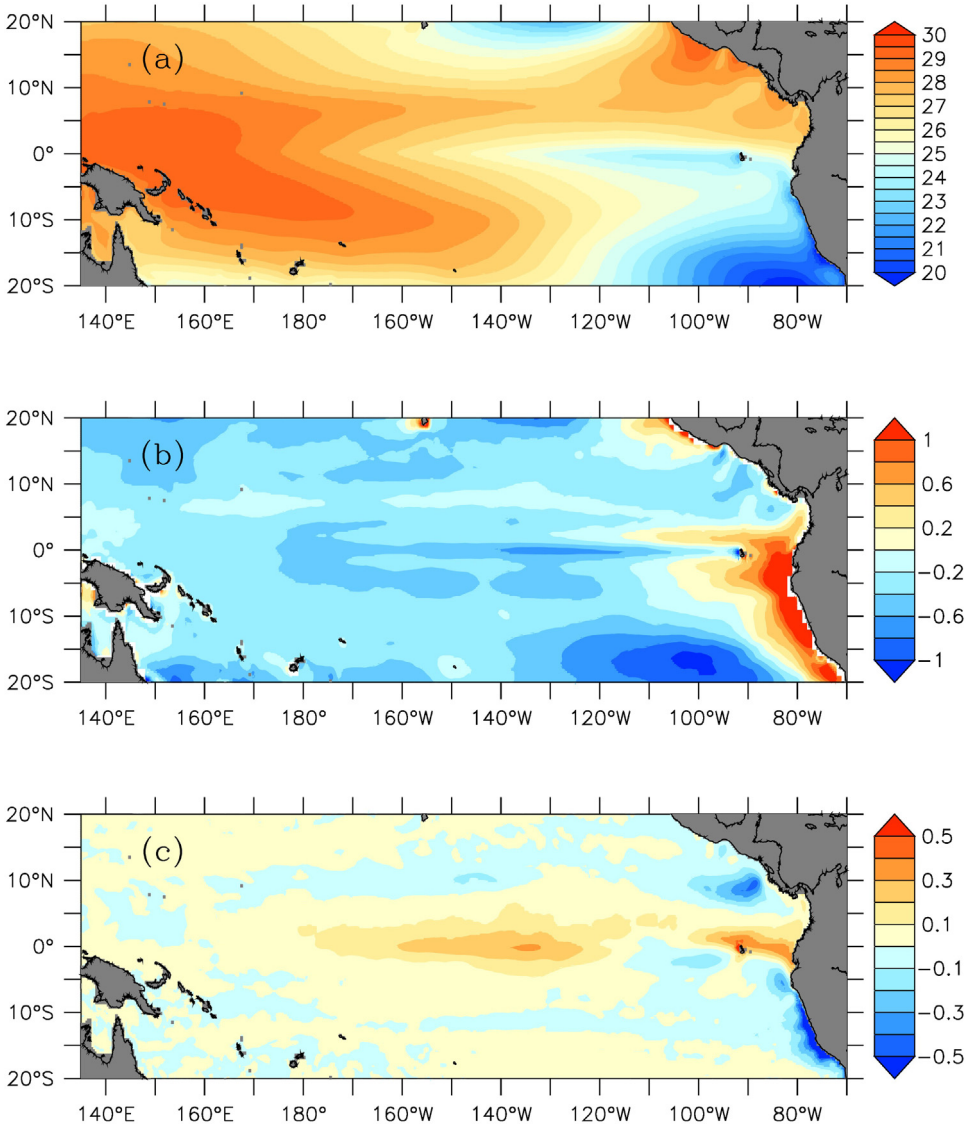

Fig. 1. (a) Temperature (°C) of the upper-most layer (taken as SST) in the low vertical resolution experiment, (b) the difference between (a) and SST from the ECMWF Interim, and (c) SST difference between the high and low vertical resolution experiments, all averaged over 40 years (1979–2018).

Causes of the warm bias off the South American coast have been investigated by a number of studies as summarized in Zuidema et al. (2016), identifying inadequacies in the representation of low-level clouds, convection, and winds in the atmospheric component, and thermocline structure in the ocean component, among others. It is also recognized that model resolution in both the atmosphere and ocean is often a limiting factor in resolving the relevant processes in the climate models currently in use.

The message is clear from the studies mentioned above and many more that SST biases originate in both the ocean and the atmosphere components of a coupled model; an error in one component can lead to errors in the other; and these errors may be amplified through the strong coupling between the atmosphere and ocean.

Ocean mixing plays an important role in modulating the temperature in the upper ocean. Observational studies show that ocean mixing exerts strong controls on the seasonal cycle of SST (Moum et al., 2013) and is actively involved in the phase transitions of the El Niño-Southern Oscillation (ENSO; Warner and Moum, 2019) at 140°W, equator. In ocean models, equatorial Pacific SST is highly sensitive to the specification of vertical mixing (e.g. Jochum, 2009; Richards et al., 2009; Zhu and Zhang, 2018, 2019). Along the equatorial Pacific, the application of a low background vertical diffusivity, a parameterization of ocean mixing by unresolved processes, usually leads to a warmer cold tongue, through the sharpening of the thermocline. Meehl et al. (2001) showed that models with a colder than observed temperature in the upper ocean tend to have a too shallow thermocline even though they may produce the observed thermocline intensity (and El Niño amplitude) at low vertical diffusivity. Naturally, an important prerequisite to reducing SST bias must be a realistic thermocline structure, both its thickness and its depth. Jia et al. (2015) undertook a systematic study of the impact of vertical diffusivity on the temperature structure of the equatorial Pacific Ocean. They found that the depth and the thickness of the equatorial pycnocline (thermocline) can be altered by varying the vertical diffusivity with depth. With ocean-only model experiments, Sasaki et al. (2012) demonstrated that an enhancement of the background vertical diffusivity within and above the thermocline both sharpens and deepens the thermocline, and the cool bias of the cold tongue is reduced as a result. This effect is amplified in a coupled atmosphere-ocean model (Sasaki et al., 2013) through the Bjerknes feedback and SST-shortwave flux feedback (Klein and Hartmann, 1993).

The modeling studies by Sasaki et al. (2012, 2013) were motivated by measurements taken in the western equatorial Pacific (Richards

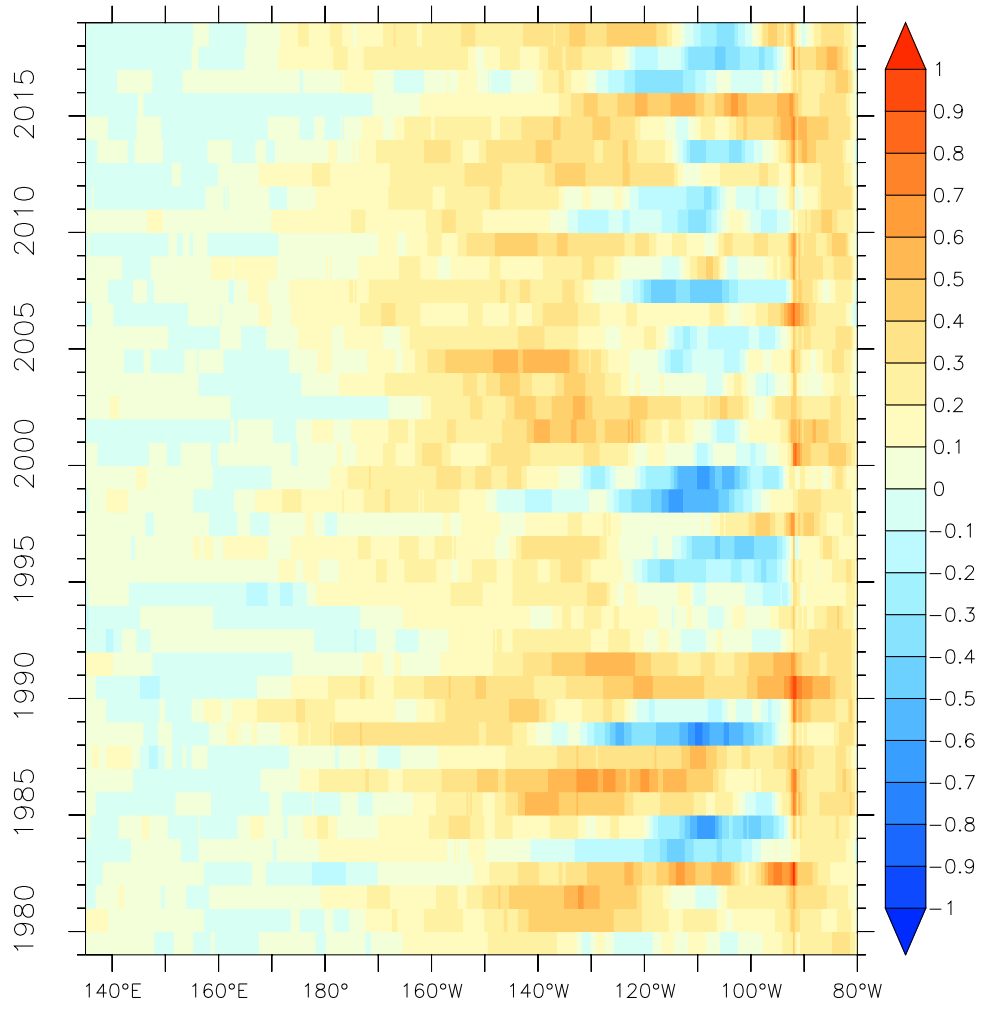

Fig. 2. Annual-mean SST difference (°C) between the high and low vertical resolution experiments along the equator (1°S-1°N average).

et al., 2012, 2015). Vertical velocity shear was observed to be dominated by flow features with small vertical scales (~20–50 m), contributing to an increase in vertical mixing within and above the thermocline. In the eastern equatorial Pacific (the cold tongue region), enhanced mixing in the thermocline has also been observed. From Argo float and the Tropical Ocean and Atmosphere (TAO) mooring measurements, Liu et al. (2016, 2019b) identified numerous mixing events in the thermocline and attributed them to low Richardson numbers resulting from shear associated with Tropical Instability waves (TIWs) and the equatorial undercurrent (EUC). Furthermore, Liu et al. (2019a, 2020) found small vertical scale (10–50 m) shear induced by the interaction between the equatorial current system and equatorial waves of different dynamic types and multiple time scales in the upper thermocline. Energetic motions with a vertical wavelength of 40 m, referred to as a "shear wave", was reported by Peters et al. (1991) from observations taken on and off the equator along 140°W in April 1987 during the second cruise of the Tropic Heat program.

The large impact on the climate system shown by Sasaki et al. (2013) from a simple parameterization of vertical diffusivity warrants a further investigation into the characteristics of vertical mixing along the whole extent of the equatorial Pacific, in particular, the contribution from shear at different vertical length scales. In this study, we address this issue by conducting numerical experiments with an ocean model at two vertical resolutions, one that is comparable with those in many ocean models currently in use, and the other that is significantly finer in the upper ocean. Through the use of a Richardson number based scheme and by specifying a low background value for the vertical diffusivity, the contribution to mixing from resolved shear at different vertical resolutions of the model experiments can then be compared and contrasted. The present research may be considered as an extension of the two-part study by Furue et al. (2015) and Jia et al. (2015). We apply the analysis method developed in Furue et al. (2015) to examine the difference in temperature structure, and relate the difference to the change in the mixing structure resulting from an increase in vertical resolution based on the key findings of the two-part study.

The details of our experimental design are described in Section 2. We present our results in Section 3, making connections among the changes in SST, subsurface temperature, vertical mixing structure, stratification, and vertical velocity shear, as a result of an increase in vertical resolution. We summarize and discuss our results and provide concluding remarks in Section 4.

2. Experimental design

We use a version of the Massachusetts Institute of Technology general circulation model (MITgcm; Marshall et al., 1997), which solves the incompressible Navier–Stokes equations discretized into finite volumes on a sphere. The model configuration is an adaptation of that used by Furue et al. (2015) and Jia et al. (2015) for the tropical Pacific with minor modifications. The meridional extent of 26°S–30°N is maintained while the western boundary of the domain is extended westward to 32°E to include the tropical Indian Ocean for studies in the Maritime Continent region and the Bay of Bengal. Ocean depth is derived from the ETOPO2 database (http://www.ngdc.noaa.gov/mgg/

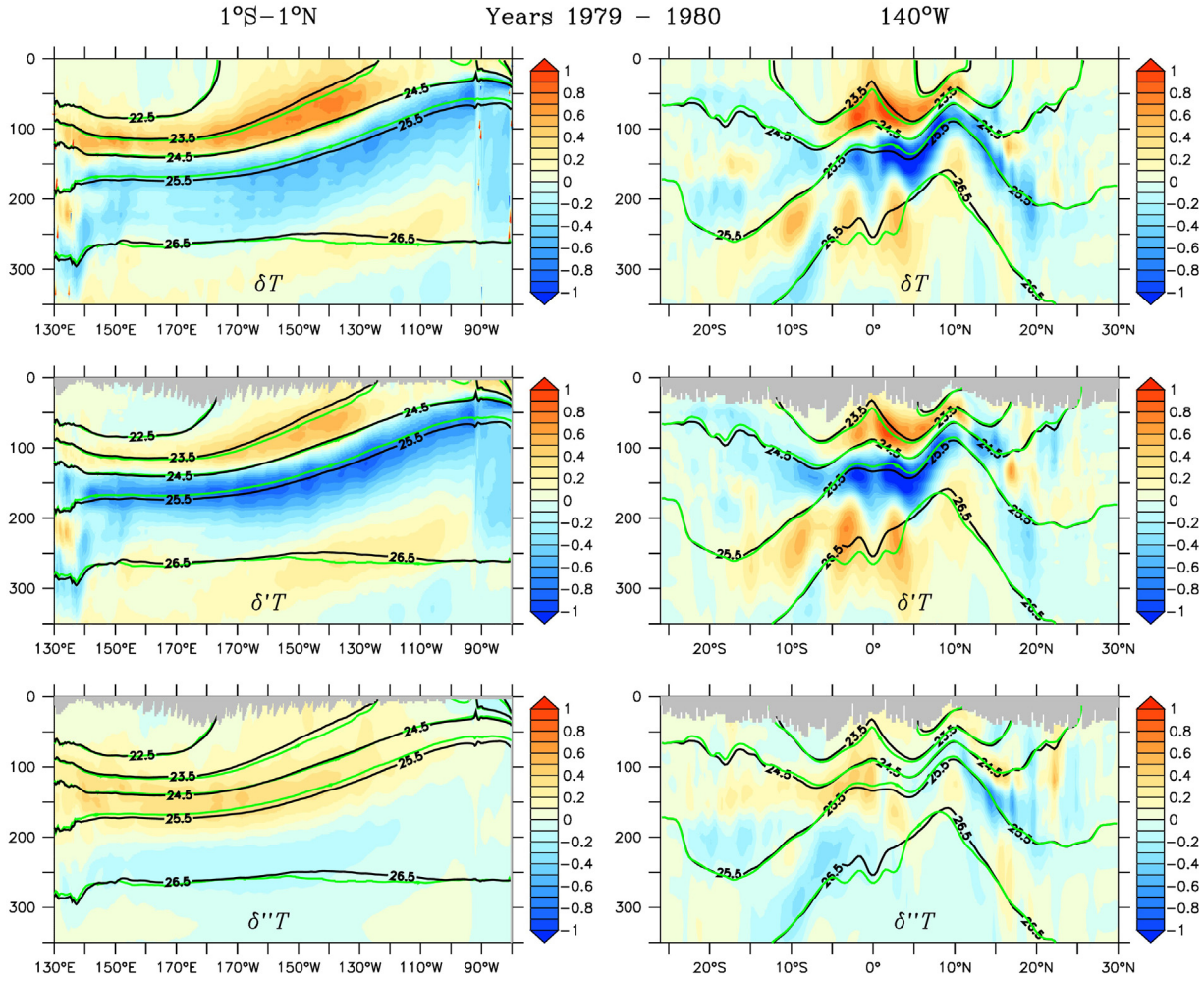

Fig. 3. Temperature anomaly (δT, °C, color), and its dynamic ($\delta' T$) and spiciness ($\delta'' T$) components, averaged over the first two years (1979–1980) along the equator (1°S-1°N average) and 140°W, overlaid with potential density (σ_θ) contours from the low vertical resolution experiment (black) and the high vertical resolution experiment (green). Light grey shading near the surface indicates regions where there are no matching density surfaces between the two experiments for decomposition.

global/etopo2.html), with the continental boundaries determined by the 10-m bottom contour. The model grid has a constant resolution of 1/3° in both the zonal and meridional directions. In the vertical direction, two schemes of discretization are used: one with 51 layers and the other 187 layers. The former has thicknesses ranging from 5 m in the upper 20 m to 510 m near the bottom, and the latter from 3 m throughout the upper 402 m to 510 m for the deepest layer. For simplicity, we shall refer to the two schemes as low and high resolutions even though the low resolution is comparable to those in many ocean models presently in use (e.g. Griffies et al., 2009). The increase from low to high resolutions is modest near the surface but is significant in the pycnocline and below. For example, the layer thickness in the depth range of 50–400 m varies from 10 to 30 m with an average around 21 m in the low resolution, in contrast to a constant of 3 m in the high resolution.

Subgrid-scale horizontal mixing is parameterized by bi-harmonic operators with constant coefficients of 3×10^{11} m^4 s^{-1} for viscosity and 2×10^{10} m^4 s^{-1} for tracer diffusion. Vertical mixing is specified with the K-profile parameterization (KPP) of Large et al. (1994) in which the background coefficients are set to 1×10^{-6} m^2 s^{-1} for both viscosity and diffusivity. In the stratified ocean interior below the surface boundary layer, the background coefficients in KPP as implemented in the MITgcm represent the part of mixing from unresolved internal wave activities. Additionally, two more contributions are included in the ocean interior, one from convective events when the stratification becomes unstable ($N^2 < 0$ where N is the Brunt-Väisälä frequency), and another from resolved vertical shear when the local gradient Richardson number, Ri, is smaller than a predefined critical value (0.3 in our experiments). The maximum values for the coefficients are set to 1×10^{-1} and 5×10^{-3} m^2 s^{-1} for the convective and shear components, respectively. Effect of double diffusion is not included.

The model uses the bulk formulae of Large and Pond (1981, 1982) to compute the turbulent fluxes of momentum, heat and fresh water at the ocean surface. The necessary atmospheric variables come from the European Center for Medium Range Weather Forecasts (ECMWF) Interim reanalysis (Dee et al., 2011) at a resolution of 1.0°. The wind components at 10 m are at 6-hourly frequency. Other variables, including radiative heat fluxes (net shortwave and downward longwave), air temperature at 2 m, specific humidity at 1000 millibar and precipitation, are averaged to daily values. Using these 6-hourly and daily fields from the period of 1 January 1979 to 31 December 2016, we generate a monthly climatology for our spin-up experiment (see below). We also make use of SST from the same database for comparison with model SST (Section 3.1).

For the open boundaries at 26°S and 30°N, model variables (temperature, salinity and horizontal components of velocity) are defined by a monthly climatology generated from the German partner of the consortium for Estimating the Circulation and Climate of the Ocean (GECCO) reanalysis (Köhl et al., 2007; Köhl and Stammer, 2008). Along each of the boundaries, a buffer zone of 3° in width (or 9 grid intervals)

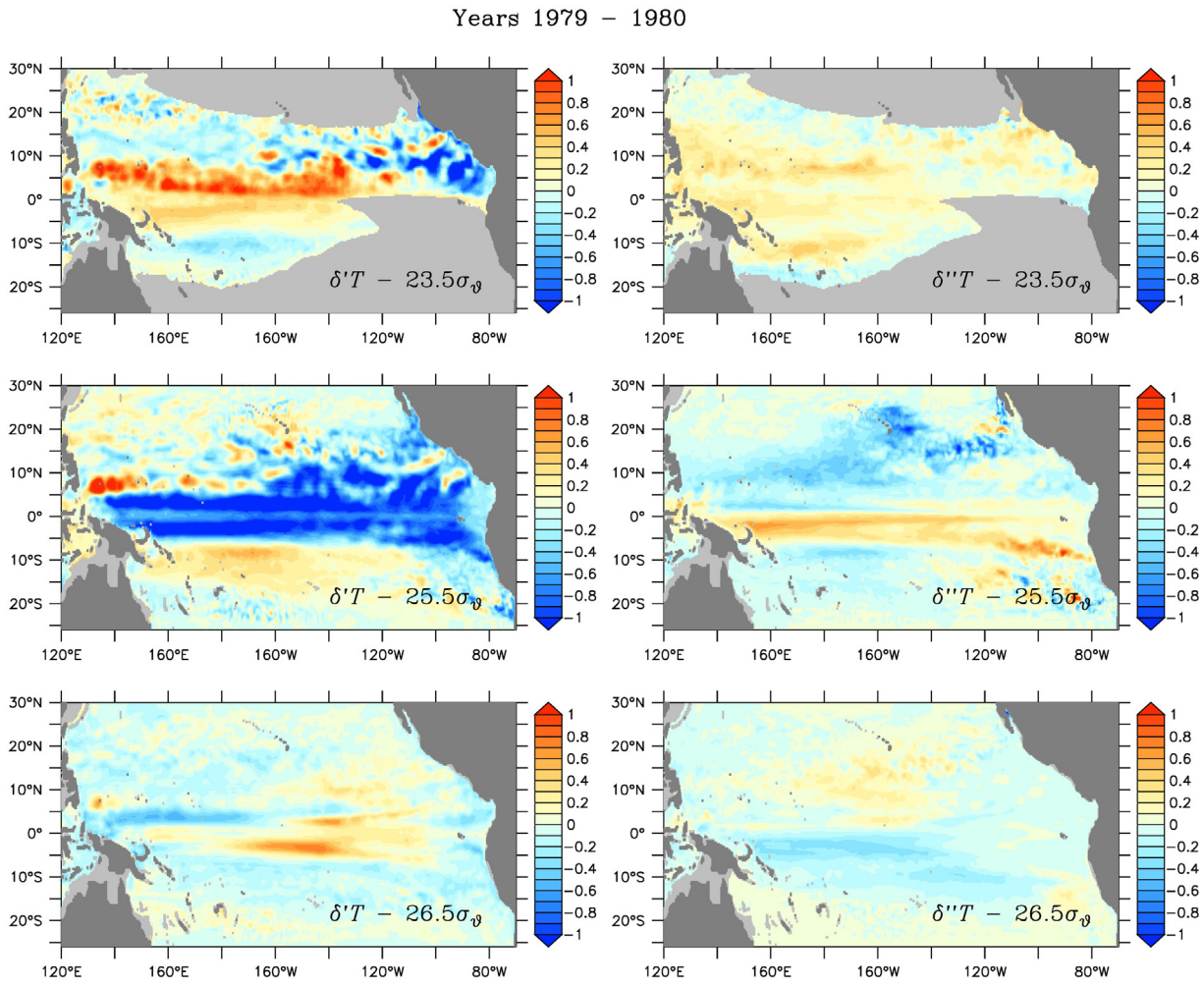

Fig. 4. Components of temperature anomaly (°C) averaged over the first two years (1979–1980) on representative potential density surfaces.

is applied for model variables to transition from the GECCO values at the boundary to that of the interior by way of restoring with time scales varying from 1 day to 20 days. This is the same procedure as that used by Furue et al. (2015) and Jia et al. (2015) for the tropical Pacific except that there is no longer the need for an open meridional boundary in the Indian Ocean with the westward extension of the domain.

The model is initialized with the climatological January state of GECCO reanalysis, and a spin-up integration of 40 years is performed at low vertical resolution forced at surface with the monthly climatology of ECMWF Interim. The end state of the spin-up experiment is then used to initialize two experiments at low and high vertical resolutions. While the low vertical resolution experiment can simply continue from the end state of the spin-up, vertical interpolation of the spin-up variables and GECCO variables is needed for initialization and open boundary conditions for the high vertical resolution experiment. We apply a linear scheme for the interpolation. Both the experiments are integrated for 40 years forced at the surface with the 6-hourly and daily ECMWF Interim variables for the period of 1979–2018.

We examine the effects of increased vertical resolution on ocean temperature by taking the difference between the two experiments using the low resolution as reference. As in Furue et al. (2015), this temperature difference, also referred to as temperature anomaly, δT, is separated into dynamical and spiciness components, $\delta' T$ and $\delta'' T$, respectively. Below the directly forced ocean surface layer, the two components have distinct properties. $\delta' T$ is generated by a pressure anomaly associated with the vertical displacement of density surfaces and is propagated by ocean waves. $\delta'' T$ is always accompanied by a compensating salinity anomaly in such a way that they do not result in a change in density and is advected like a passive tracer by ocean flows. A detailed description on the precise definitions, calculation methods and physical properties of the two components can be found in Appendix A of Furue et al. (2015), and an illustration of their pathways in the tropical Pacific is shown in their Fig. 10.

3. Results

In this section, we show that the increase in vertical resolution in our model experiments does indeed reduce the cool SST bias in the equatorial cold tongue (Section 3.1) through warming in the upper pycnocline (Section 3.2) as the result of a change in the vertical mixing structure (Section 3.3) in the central region. Additionally, in the far eastern region, a change in the vertical mixing structure produces cooling in the lower pycnocline that reduces the warm SST bias along the South American coast. The increased vertical resolution captures the small-scale vertical velocity shear and resolves the fine details of the stratification in the upper ocean (Section 3.4), contributing to the changes in the vertical mixing structure.

3.1. SST

Our reference (the low vertical resolution) experiment is essentially the same as the control run used by Furue et al. (2015) in which a comparison was made between modeled and observed fields along 160°W (see their Fig. 2). The annual mean zonal component of velocity,

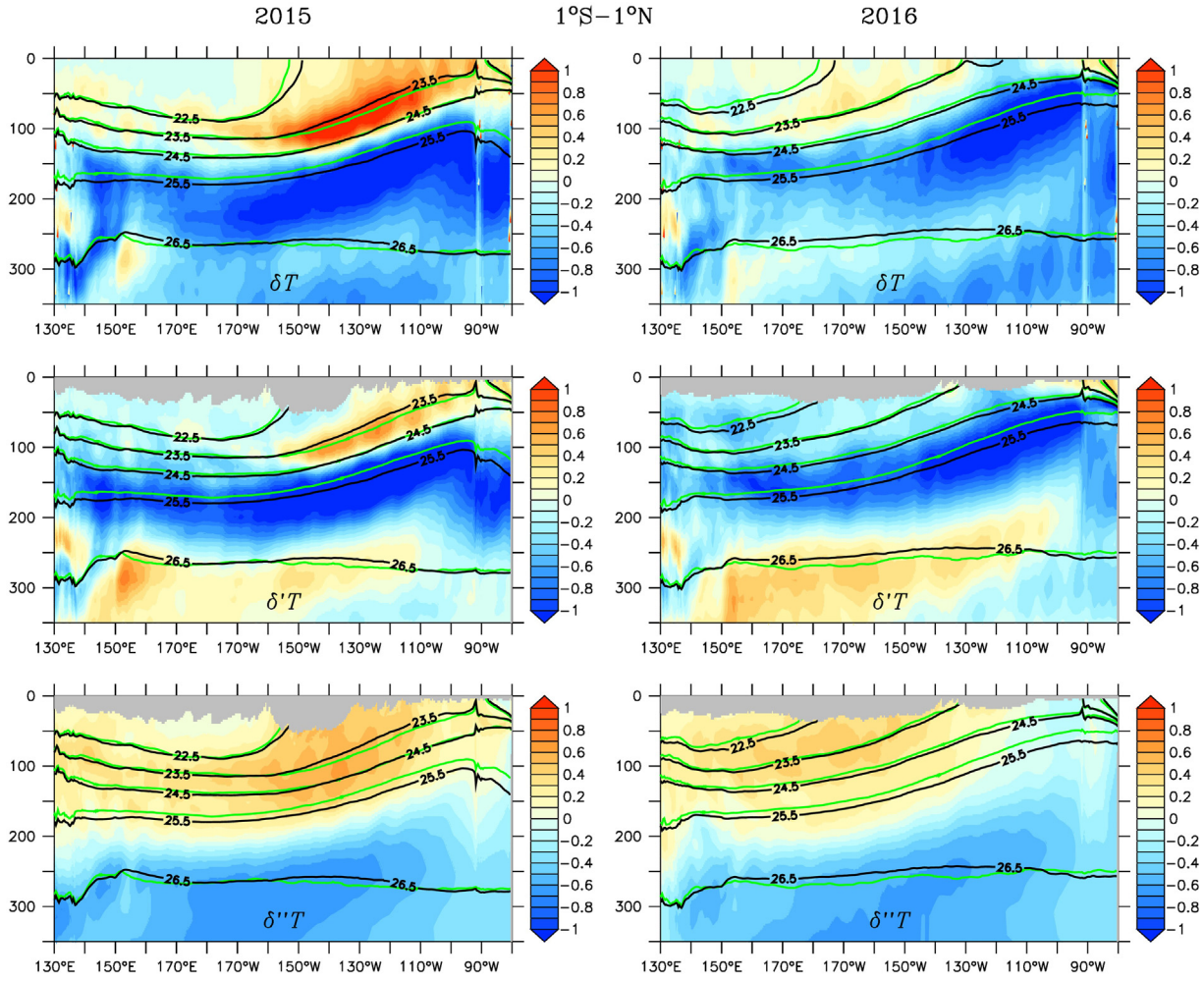

Fig. 5. Annual-mean temperature anomaly (°C) and its components along the equator (1°S-1°N average) for 2015 and 2016.

salinity and potential density were found to agree well in their large-scale features. These conclusions apply to our reference experiment as well. Since SST is the primary focus of this study, we show in Fig. 1(a) the temperature of the upper most layer (taken as SST) in the reference experiment, (b) the SST bias in the reference experiment relative to the ECMWF Interim (observation-based estimates), and (c) the SST difference between the high and low vertical resolution experiments, all averaged over 40 years (1979–2018). The large-scale features of the tropical Pacific SST are well reproduced in the reference experiment (Fig. 1a), including the warm pool in the west, the equatorial cold tongue in the east, and the contrast of warm and cool surface waters to the north and south of the equator off the west coast of the American continent. When compared with the ECMWF Interim, we see the familiar biases that commonly occur in ocean models as discussed in the introduction: a basin wide cool bias, most pronounced in the equatorial cold tongue and the subtropical regions (15-20°S and 20-30°N, the latter is not shown), and an intense warm bias along the South American coast (Fig. 1b). The cool bias reaching 0.6°C on the equator near 130°W, and the warm bias just over 1°C off the South American coast are within the ranges of those seen in ocean models (e.g. Griffies et al., 2009) and coupled atmosphere-ocean models (e.g. Burls et al., 2017).

The increase in vertical resolution alleviates the general cool bias of the domain and the warm bias along the South American coast (Fig. 1c). One of the notable effects from the increase in the model's vertical resolution is the equatorial warming in excess of 0.3°C, correcting about 50% of the cold tongue bias. There is a considerable interannual variability that is closely correlated with the phases of ENSO as shown in Fig. 2. During strong El Niño events (e.g. 1982–83, 1987–88, 1991–92, and 2015–16), warming in the eastern equatorial Pacific is much enhanced in the developing phase followed by increased cooling in the recovering phase. An exception is the 1997–98 event when the warming is only modestly enhanced but the actual event is strong in the model solutions. Fig. 2 also shows that increased cooling tends to occur during La Niña events (e.g. 1988–89, 1999–2000, and 2010–11).

Comparing (b) and (c) of Fig. 1, we see that the increase in vertical resolution also increases existing biases, specifically the warm bias to the east of the Galapagos Islands (near 90°W, equator), and the cool bias at the Costa Rica dome (near 90°W, 10°N). In Section 3.3, we show that the equatorial warming and the coastal cooling off the equator seen in Fig. 1c share the same cause — a change in the vertical mixing structure.

3.2. Subsurface temperature

Fig. 3 displays the temperature difference between the high and low vertical resolution experiments (δT) and its components averaged over the first two years (1979–1980) along the equator (1°S-1°N average) and 140°W, overlaid with potential density contours from the reference experiment (black) and the high vertical resolution experiment (green). Here we choose a time average of two years to allow the effects of change in vertical resolution to develop (see Fig. 2). At this initial phase, much of the difference happens within 10° of the equator.

Along the equator (Fig. 3, left), there is a layered distribution of positive, negative and positive anomalies in the upper, lower and below

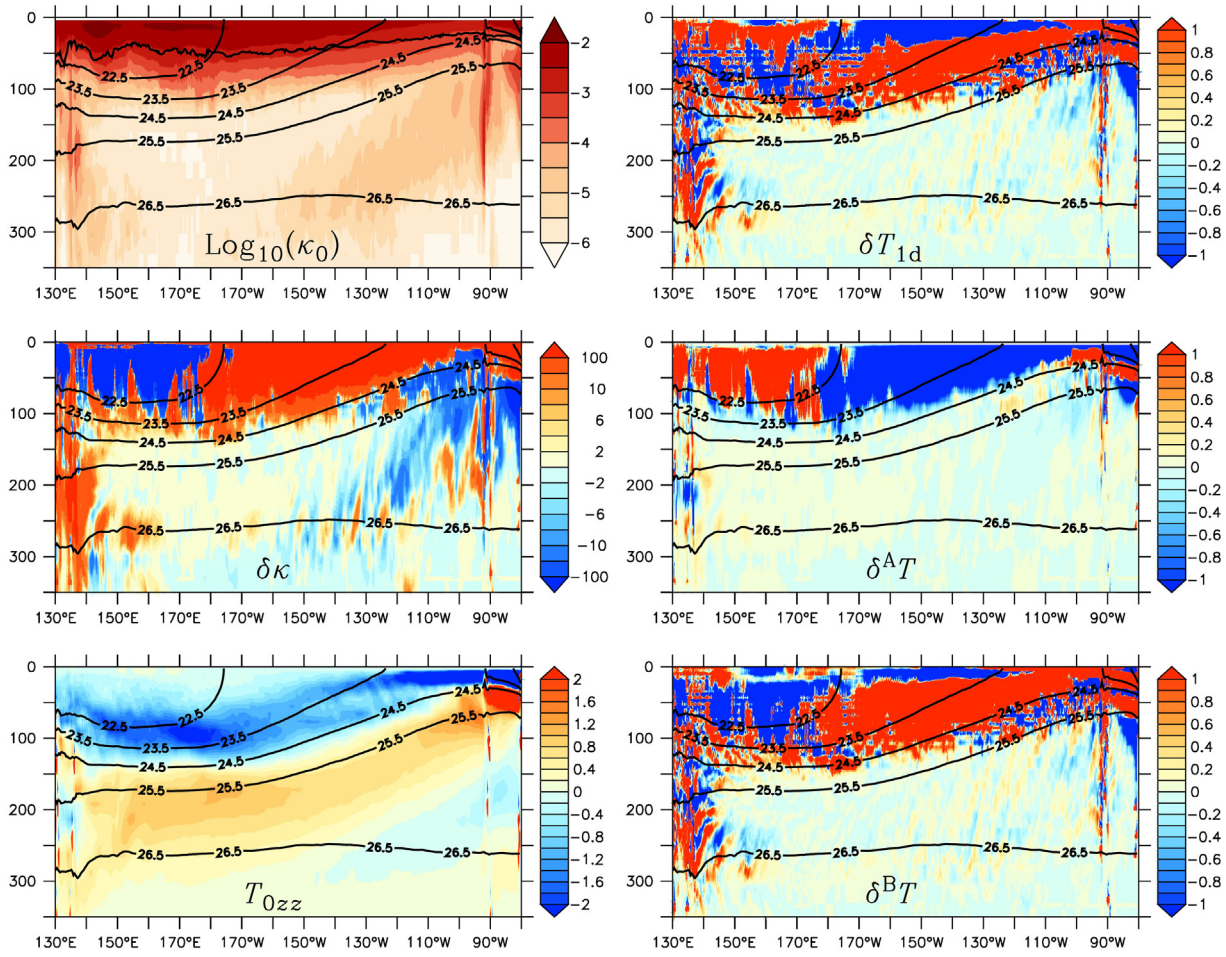

Fig. 6. Various fields in the 1-d diffusion equation along the equator (1°S-1°N average) evaluated using the low vertical resolution experiment as reference and the difference in vertical diffusivity between the two experiments, overlaid with σ_θ contours (black) from the reference experiment. The fields are averages over the first two years (1979–1980). The black curve in the upper-left panel with no labels indicates the maximum surface boundary layer depth in the ranges of 1°S-1°N and 1979–1980. Units: $m^2\ s^{-1}$ for κ_0, 1×10^{-6} $m^2\ s^{-1}$ for $\delta\kappa$, 1×10^{-3} °C m^{-2} for T_{0zz}, and °C for temperature anomalies.

the pycnocline, respectively. This pattern comes primarily from the dynamical component ($\delta' T$). The shift of the green contours towards the middle of the pycnocline (approximated by the 24.5 σ_θ) relative to the black contours suggests a tightening of the pycnocline in the high vertical resolution experiment. Consistent with its definition, $\delta' T$ attains positive and negative signs in the upper and lower parts of the pycnocline, respectively. The deeper positive $\delta' T$ results from the deepening of the 26.5 σ_θ. The spiciness component ($\delta'' T$) is positive in the pycnocline and weakly negative below. The upper pycnocline rises to the surface in the central and eastern regions, bringing positive anomaly from both the components to increase SST there.

Along 140°W, it appears that the positive-negative-positive layers of $\delta' T$ on the equator are bordered by stronger anomalies just off the equator (Fig. 3, middle-right). Maps of $\delta' T$ on representative density surfaces (Fig. 4, left panels) show that this is likely the case for the two positive anomalies (23.5 and 26.5 σ_θ). For the negative anomaly (25.5 σ_θ), off-equatorial influence is evident. As discussed in Furue et al. (2015), the dynamical anomaly generated in the off-equatorial regions propagates westward as Rossby waves, then equatorward as coastal Kelvin waves, and then eastward along the equator as equatorial Kelvin waves. The extension of the weaker negative $\delta' T$ from the western boundary on 25.5 σ_θ suggests a stronger background negative $\delta' T$ modified by a positive $\delta' T$ coming from the western boundary. There is plenty of positive $\delta' T$ on this density surface that converges at the western boundary and enters the equatorial waveguide. Anomalies in the off-equatorial regions enter the equatorial waveguide on other density surfaces too. As will be discussed later (last paragraphs of this and next sections), $\delta' T$ in the western equatorial region on 23.5 σ_θ experiences large changes during the time period of the experiments, as a result of influences from the off-equatorial regions. For the 26.5 σ_θ, on the other hand, the positive $\delta' T$ along the equator is locally generated and appears to withstand negative influences from the west.

Within the pycnocline, the spiciness anomaly ($\delta'' T$) along the equator is advected eastward in the EUC (Fig. 3, lower-left). The spiciness anomaly in the off-equatorial regions can also reach the equator following the subsurface branches of the STCs. The precise advective pathways differ in the two hemispheres as shown in (Furue et al., 2015, their Fig. 10). For example, the positive $\delta'' T$ on 25.5 σ_θ (Fig. 4, middle-right) in the southern hemisphere can reach the EUC either directly in the middle of the ocean basin or by flowing first to the western boundary and then to the equator in the New Guinea coastal current. Since part of this coastal current crosses the equator, it brings the southern positive $\delta'' T$ into the EUC on both sides of the equator. In contrast, the negative $\delta'' T$ in the northern hemisphere cannot reach the EUC directly in mid-basin because of the presence of the North Equatorial Countercurrent (NECC). Instead it flows to the western boundary in the North Equatorial Current (NEC), then equatorward in the Mindanao Current, and then eastward in the NECC and along the northern flank of the EUC (thus not crossing the equator).

As time advances, the interannual variability reflected in Fig. 2 at the surface is tightly linked to subsurface changes. Here we use the 2015/16 El Niño event (Hu and Fedorov, 2016; Levine and McPhaden,

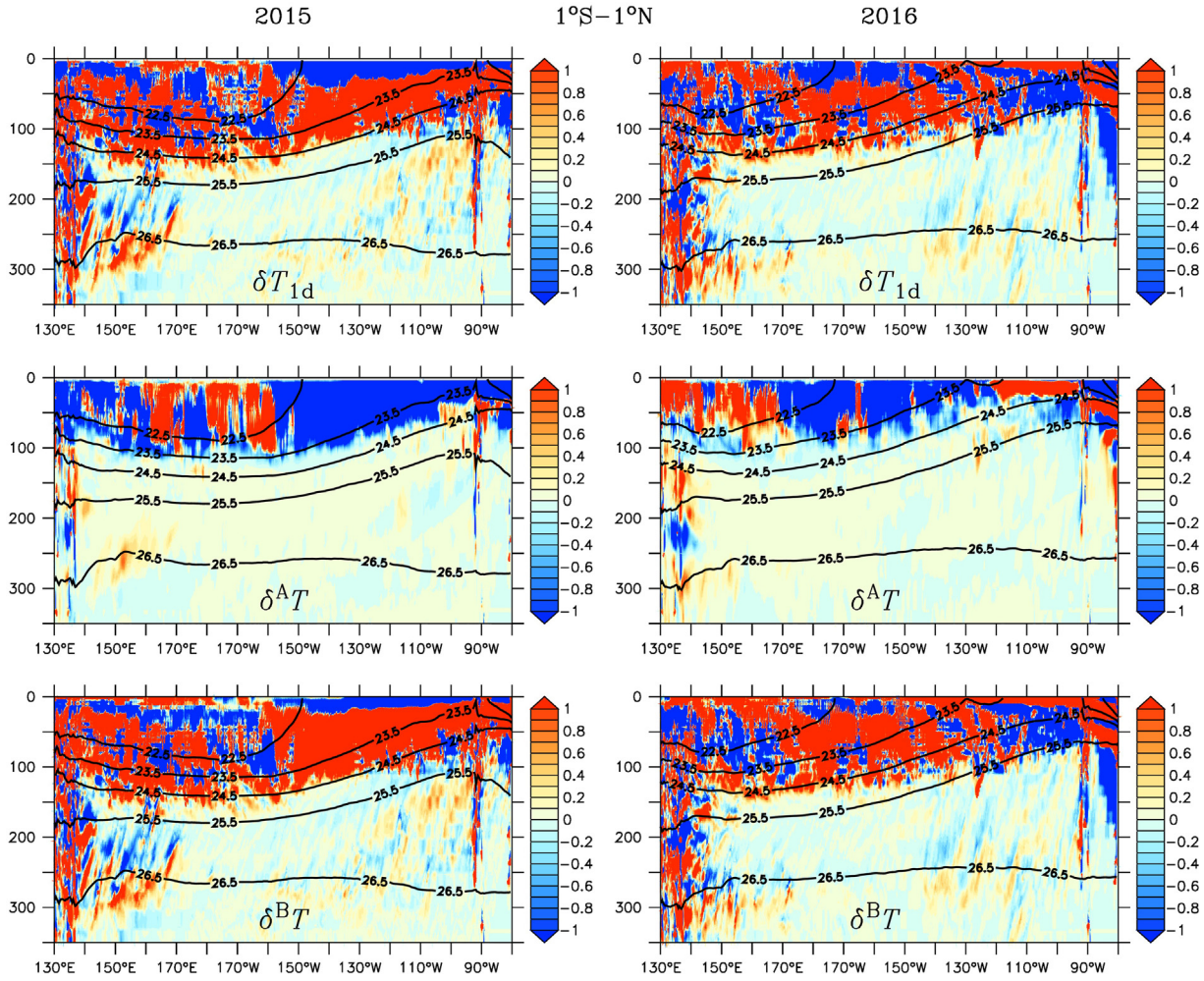

Fig. 7. Annual-mean temperature anomaly (°C) based on the 1-d approximation and its components along the equator (1°S-1°N average) for 2015 and 2016.

2016; Zhang and Gao, 2017) as an example. Fig. 5 shows the contrasting states during the developing phase (2015) and the recovering phase (2016) along the equator. With the deepened and also tightened pycnocline in the eastern sector during the developing phase, the upper positive $\delta' T$ is significant, and the positive $\delta'' T$ is strong, together they increase SST. During the recovering phase, there is no longer an upper positive $\delta' T$, and the pycnocline shoals sharply toward the east to reach the surface in the eastern sector, bringing negative $\delta' T$ to the surface to lower SST there. $\delta'' T$ also appears to be much weakened with the maximum shifted westward and a sign reversal near 100°W.

The high connectedness of the equator with the off-equatorial regions means that changes along the equator can also influence the rest of the basin in the tropical Pacific. The characteristic shape of the negative $\delta' T$ on 25.5 σ_θ in the eastern basin (Fig. 4, middle-left), fanning out towards the eastern boundary (see Furue et al., 2015 for more examples), is typical of an anomaly carried by a series of propagating waves: eastward equatorial Kelvin waves, poleward coastal Kelvin waves, and then westward Rossby waves reflected off the eastern boundary. In later years of the model experiments, the negative $\delta' T$ is much enhanced and the characteristic shape is more clearly defined in the domain (not shown). Most importantly, this subsurface negative $\delta' T$ spans a wide density range at the eastern boundary (Fig. 3, middle-left; Fig. 5, middle panels). These density surfaces outcrop in the southeastern region, bringing the negative $\delta' T$ to cool the surface off the South American coast (Fig. 1c).

Similarly, the positive $\delta' T$ at the surface next to the eastern boundary (east of Galapagos Islands near 90°W), though shallow, is persistent (Fig. 3, middle-left; Fig. 5, middle panels), and we may reasonably conclude that the warm SST bias along the eastern boundary in the equatorial region (Fig. 1c) results from its propagation via coastal Kelvin waves. Its southward extension along the South American coast ends where it meets denser surface waters. Its northward extension ends where it meets the negative $\delta' T$ at the Costa Rica dome.

The cooling at the Costa Rica dome near 90°W, 10°N (Fig. 1c) occurs on lighter densities (<24.5 σ_θ) thus cannot originate from the lower pycnocline at the equator. In this area, there is a negative $\delta' T$ at the surface and in the upper pycnocline (e.g. Fig. 4, upper-left), which grows with time and propagates westward as a Rossby wave. The anomaly reaches the western boundary and enters the equator, dominating or reducing locally generated anomalies along its pathway (comparing Fig. 3, middle-left with Fig. 5, middle panels, 23.5 σ_θ). Its westward extension at the surface is limited because the affected densities are below the surface away from the domed region.

3.3. Vertical diffusivity

The decomposition of δT into dynamical and spiciness components is useful for understanding the behavior of the difference because of the distinct ways with which the two components spread in the ocean. It is not always possible, however, to identify the source of an anomaly since δT at any given location is determined by a combination of local and remote effects. Based on the characteristics of δT distribution in the study domain, here we make an attempt to deduce certain causes and effects by applying knowledges gained from prior studies.

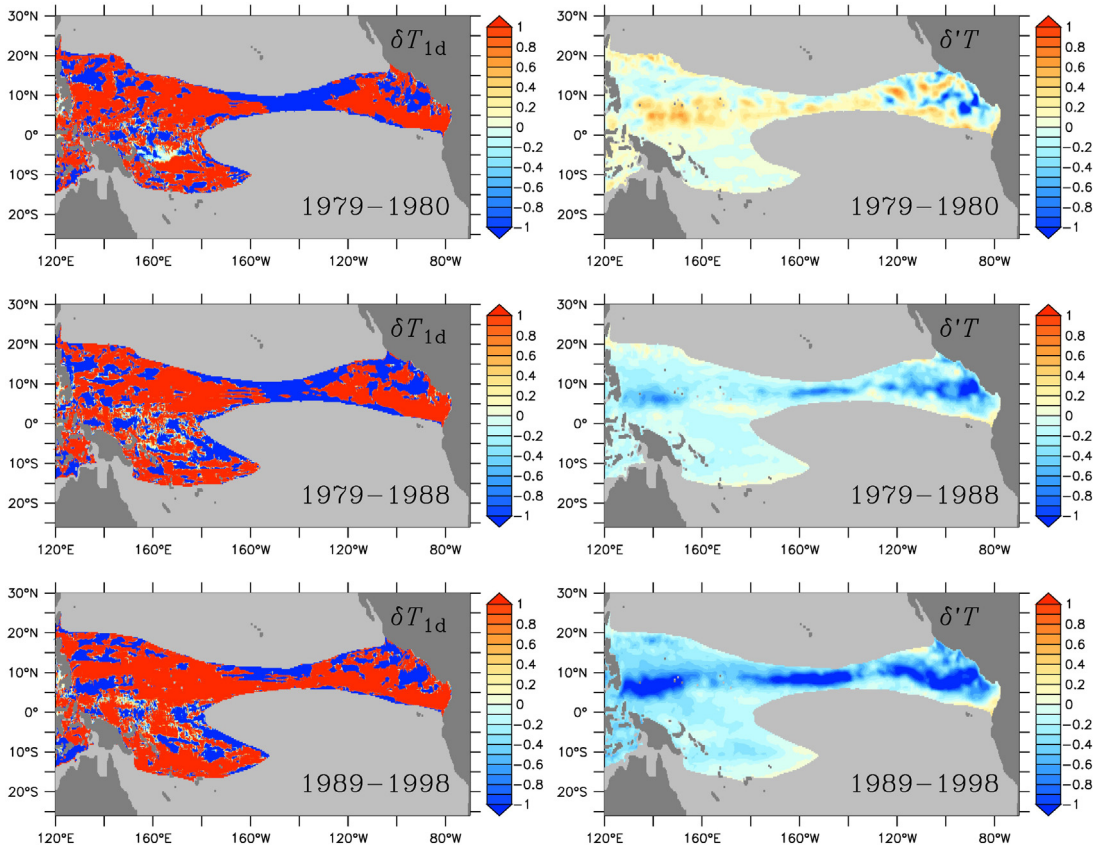

Fig. 8. Temperature anomaly (°C) on potential density surface $\sigma_\theta = 22.5$ based on the 1-d approximation and the dynamical component, averaged over the years as indicated.

Furue et al. (2015) and Jia et al. (2015) explored the impacts of vertical diffusion on the temperature structure of the equatorial Pacific by conducting numerical experiments in which the background vertical diffusivity, κ_b, was changed each time only in one subregion of the tropical Pacific. They found that the initial response of δT follows closely the one-dimensional (1-d) balance of vertical diffusion within the forced region (where κ_b is changed). Considering the two leading terms only, the 1-d equation of temperature anomaly can be written as

$$\delta T_{1d} = \delta\kappa T_{0zz} t + \delta\kappa_z T_{0z} t = \delta^A T + \delta^B T$$

where $\delta\kappa$ is the change in vertical diffusivity relative to the reference value κ_0, T_0 is the temperature of the reference experiment, subscript z represents the vertical derivative of a variable, and t is the time scale that the above balance is assumed to be valid. $\delta^A T$ represents the response primarily to a change in the vertical diffusivity, whereas $\delta^B T$ is associated with the vertical variation of the change in vertical diffusivity.

Strictly speaking, the full vertical diffusivity, consisting of the background value, the convective part and the shear-dependent part in the KPP scheme, should be used. In Furue et al. (2015) and Jia et al. (2015), only the change in κ_b is considered in evaluating $\delta^A T$ and $\delta^B T$ for simplicity. This is in fact a very good approximation since κ_b is sufficiently large in the ocean interior in their experiments and the additional parts are generally inactive. For the two experiments discussed in this study, however, the difference is in the convective and the shear-dependent parts since the same background value is used for both the experiments.

Fig. 6 shows several fields in the 1-d diffusion equation along the equator (averaged over 1°S-1°N) evaluated using the two model solutions in this study. The fields are averages over the first two years (1979–1980). Similar to Fig. 3, this two-year time scale is to give adequate time for the effects of high vertical resolution on vertical diffusivity to develop.

Along the equator, the vertical diffusivity, as evaluated by the KPP scheme, in the reference experiment (κ_0), is highest in the surface boundary layer, decreases with depth to a local minimum in the pycnocline, increases moderately below the pycnocline, and then decreases again to the predefined background value of 1×10^{-6} m^2 s^{-1} at depth. The low value in the pycnocline is typical of a Richardson number based scheme as a result of high stratification combined with low shear in the core of the EUC, whereas the moderate increase below the pycnocline results from reduced stratification and increased shear in the lower part of the EUC. In the eastern basin where the lower pycnocline rises to the surface boundary layer, the subsurface minimum is not as noticeable as in the western and central regions. Bathymetric features, namely the Maritime Continent to the west of 140°E and the Galapagos Islands near 90°W, enhance subsurface mixing.

The above description holds for the high vertical resolution experiment as well. In detail, however, the change in vertical resolution generates large regional differences in vertical diffusivity. The most dramatic effects are: (1) the increase in the upper pycnocline through to the surface in the central region (positive $\delta\kappa$), (2) the reduction in the lower pycnocline in the eastern region, (3) the reduction above the pycnocline in the western region, and (4) the increase below the pycnocline (along approximately 26.5 σ_θ) across almost the whole equatorial extent.

Based on the 1-d balance, $\delta^A T$ is negative in the upper ocean in the central region resulting from the positive $\delta\kappa$ and negative T_{0zz}, an effect often seen when there is an increase in vertical diffusivity in ocean models. Almost in the same region, $\delta^B T$ is negative in the thin layer at the surface and positive below, implying negative and positive $\delta\kappa_z$, respectively, since T_{0z} is generally positive. The distribution of δT_{1d} suggests the dominance of $\delta^B T$, highlighting the importance of the vertical variation of $\delta\kappa$. In Jia et al. (2015), δT_{1d} from the 1-d diffusion equation is also decomposed into dynamical and spiciness anomalies. Because $\delta\kappa$ in this study exhibits large vertical variations,

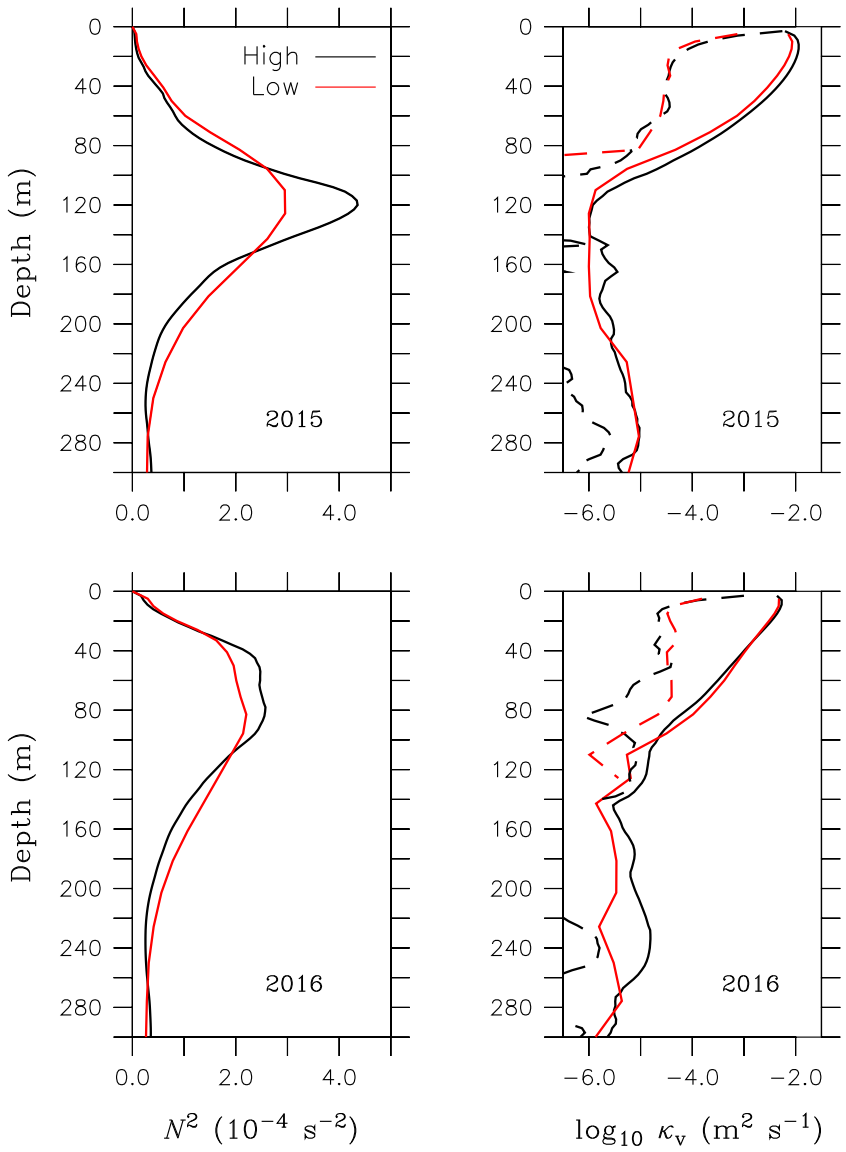

Fig. 9. Brunt-Väisälä frequency squared (N^2) and vertical diffusivity (κ_v) in 2015 and 2016 at 140°W, averaged over 1°S-1°N from the high (black) and low (red) vertical resolution experiments. Dashed curves represent contributions from the convective component.

such a decomposition is problematic. Using the results of Jia et al. (2015) as a guide (their Figs. 3 and 4), we may attribute both $\delta^A T$ and $\delta^B T$ mostly to the dynamical component along the equator. In the off-equatorial regions, the spiciness component can be significant, especially in regions where salinity has large variations such as salty South Pacific subtropical water overlying fresher deeper water.

There is a strong resemblance in the warming of the upper pycnocline in the central region between δT_{1d} generated by the positive $\delta\kappa_z$ in Fig. 6 and $\delta' T$ in Fig. 3 (middle-left). We also see an analogue of the δT_{1d} and $\delta' T$ distributions to the two left panels of Fig. 7 in Jia et al. (2015) in which κ_b increases upwards within the upper pycnocline in the western equatorial region (their experiment EQWa). Differences in the details result primarily from the positioning of the anomalies along the equator and the propagating characteristics of the dynamical anomaly. In EQWa, the surface cooling is limited to the western region because it occurs on light density surfaces that outcrop there. This is in contrast to the subsurface warming that propagates eastward away from the directly forced western region and outcrops in the eastern region. In Fig. 3 (middle-left) and Fig. 6 (upper-right), the subsurface warming outcrops in the central and eastern regions, wiping out the surface cooling to increase SST there.

Although the 1-d approximation is only defined for the initial phase, there are times when the signatures of δT_{1d} are identifiable in the later stages of the model experiments as well. Fig. 7 shows δT_{1d} and its components in 2015 and 2016. Comparing Figs. 5 and 7, there is a good correspondence between δT_{1d} and $\delta' T$ in the warming of the upper pycnocline in 2015. By contrast, the positive δT_{1d} in the upper pycnocline is not visible in $\delta' T$ in 2016, indicating a stronger influence from remote effects (see the last paragraph of this section).

The results above show clearly that the surface warming along the equator in the central region (Fig. 1c) is brought about by the warming in the upper pycnocline from a change in the structure of the vertical diffusivity. The same argument can also explain the warming at the surface east of the Galapagos Islands (~90°W) and the cooling below (24.5–26.5 σ_θ) in the eastern region (Fig. 3, middle-left; Fig. 6, upper-right). These anomalies are then carried poleward by coastal Kelvin waves to influence SST along the eastern boundary as discussed in the last section. Another effect of the subsurface cooling is the suppression of the warm layer around 26.5 σ_θ along the equator (Fig. 3, middle-left; Fig. 5, middle panels). There are positive patches of δT_{1d} in the western region (Fig. 6, upper-right; Fig. 7, upper-left) and in the eastern region (Fig. 7, upper-right) that generate the positive anomaly across almost

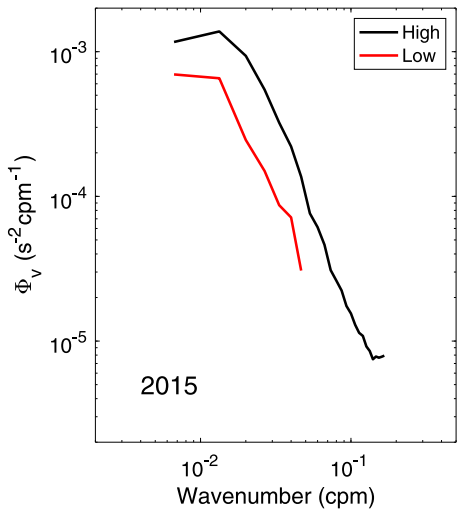

Fig. 10. Power spectra of the vertical shear of the meridional component of velocity, Φ_v, over the depth range of 50–200 m at 140°W, equator from the high (black) and low (red) vertical resolution experiments averaged over 2015.

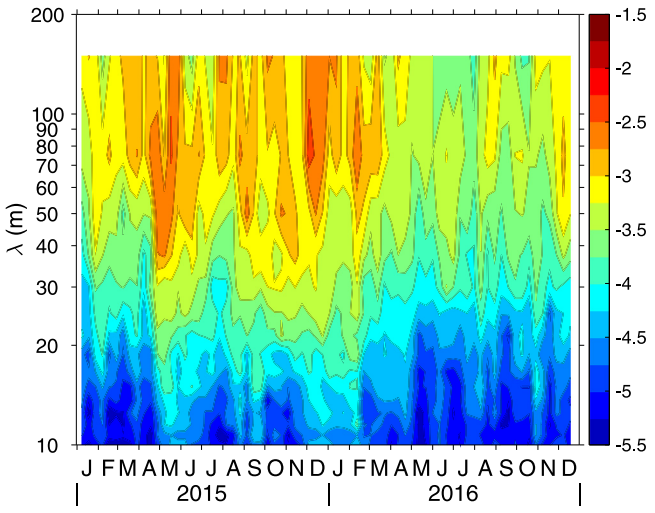

Fig. 11. Log (Φ_v, s^{-2} cpm^{-1}) as a function of time and wave length from the high vertical resolution experiment at 140°W, equator over the depth range of 50–200 m.

the whole of the equatorial extent. This positive anomaly, however, does not reach the off-equatorial regions because it is eliminated by the negative anomaly at the eastern boundary.

The cooling at the Costa Rica dome and its westward influence is a good demonstration of the competing strengths of local versus remote changes. There are patches of persistently negative δT_{1d} around 90°W, 10°N (Fig. 8, left panels). Initially, the cooling effect is evident only locally (Fig. 8, upper-right). As time progresses, its strength increases and its influence expands westward (middle and lower right panels). Along its pathway, negative $\delta' T$ is reduced in regions of positive δT_{1d} (e.g. 130°W and 170°E) and enhanced in regions of negative δT_{1d} (150°W and 140°E). On this shallow density surface (22.5 σ_θ), its influence on the equator is limited to the western region. On deeper surfaces (e.g. 23.5 σ_θ), it affects the temperature structure of the upper pycnocline to a much larger extent. During the developing El Niño in 2015, the positive δT_{1d} region (Fig. 7, upper-left) is shifted eastward and is strong enough to prevail over negative influence from the west to generate a positive $\delta' T$ (Fig. 5, middle-left); whereas during 2016, the patches of positive δT_{1d} in the central region (Fig. 7, upper-right) appear to be overcome by negative influence from the west, resulting in a negative $\delta' T$ (Fig. 5, middle-right).

3.4. Stratification and vertical shear

The analysis in Section 3.3 shows clearly that the warming along the equator and the cooling off the South American coast at the sea surface in the high vertical resolution experiment result from a change in the structure of vertical mixing in the pycnocline at the equator. Above the background vertical diffusivity which is set to the same constant in the model experiments, the KPP scheme computes the convective and shear components below the surface boundary layer based on stratification (N^2) and local gradient Richardson number (Ri), respectively. We may expect that the change in vertical resolution has impacted significantly the stratification and vertical shear (and therefore Ri). In this section, we examine the characteristics of these two quantities at 140°W and 85°W on the equator. The former is located where δT_{1d} is positive in the upper pycnocline, and the latter where δT_{1d} is negative in the lower pycnocline.

Fig. 9 (left) shows the contrast in N^2 at 140°W, equator, between the two resolutions and between 2015 and 2016. Higher vertical resolution permits a sharper pycnocline in both 2015 and 2016, but the effect is much larger in 2015 during the developing El Niño. Despite the sharp increase in stratification in 2015, above the middle of the pycnocline (maximum N^2), both $\delta\kappa$ and $\delta\kappa_z$ are positive (Fig. 9, upper-right), corresponding to negative $\delta^A T$ and positive $\delta^B T$ (Fig. 7, middle and lower left panels), respectively, suggesting that Ri in the high vertical resolution experiment is not only less than the critical value of 0.3 indicating the presence of shear-generated turbulence but also much less than that in the low vertical resolution experiment (the convective contributions, dashed curves, are similar in the two resolution). Fig. 10 displays the power spectra of the vertical shear of the meridional component of velocity, Φ_v, averaged over 2015. The enhancement of Φ_v from low to high vertical resolution is clearly evident at wave numbers lower than 0.05 cpm which is taken here as the highest possible wave number (corresponding to the lowest possible wave length of 20 m) resolved by the low vertical resolution experiment.

There is a significant temporal variability in the shear spectra in the model experiments. Fig. 11 shows Φ_v as a function of time and wave length for the high vertical resolution experiment. The values of Φ_v at all resolved length scales are higher during El Niño (March 2015–February 2016) than the months that follow. The elevated values are consistent with the elevated westerly wind activity during El Niño (see Natarov and Richards, 2019, who consider the generation of inertia-gravity waves by wind variability close to the equator). The temporal variability of Φ_v in the low vertical resolution experiment is similar to that shown in Fig. 11 but lower in amplitude.

At 85°W, equator, the pycnocline is much shallower and sharper than in the central and western regions (see Figs. 5 and 7), and maximum N^2 occurs above 40 m with a larger value in the high vertical resolution experiment (Fig. 12, left panels). Beneath the highly stratified surface layer, stratification is very weak and often becomes unstable as indicated by the significant level of convective contribution (Fig. 12, right panels, dashed curves) to the total vertical diffusivity, κ_v, in both the experiments. Note that negative N^2 is not reflected in the time-averaged profiles. The power spectra of vertical velocity shear (not shown) is similar to that at 140°W, that is, the shear intensity is higher in the high vertical resolution experiment and during the 2015–2016 El Niño. Despite the enhancement in shear with increased vertical resolution, $\delta\kappa$ is largely negative at the subsurface, suggesting that stratification plays a dominant part in determining κ_v at this location, with a larger contribution coming from the convective component in the low vertical resolution experiment ($N^2 < 0$, red dashed curves).

4. Summary, discussion, and concluding remarks

In this study, we explore the impact of vertical resolution in an ocean model in reducing SST biases in the tropical Pacific Ocean, by

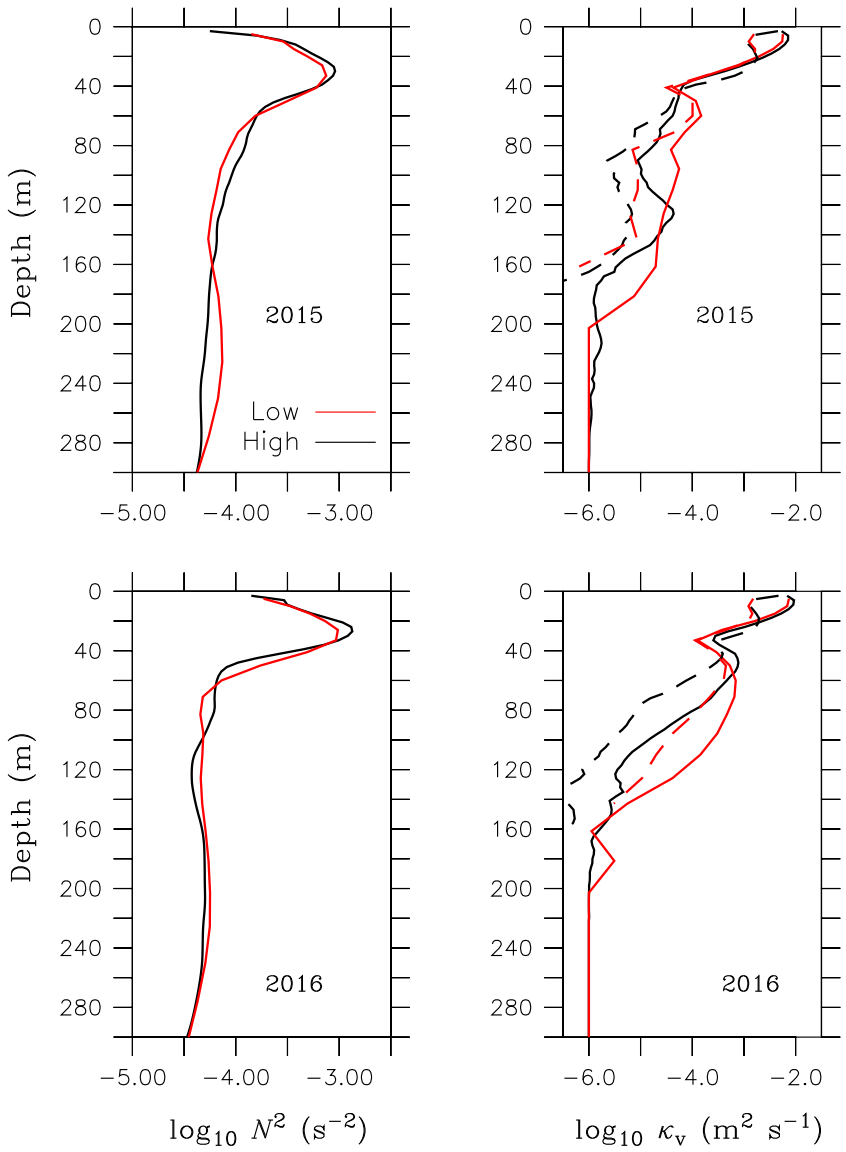

Fig. 12. Brunt-Väisälä frequency squared (N^2) and vertical diffusivity (κ_v) in 2015 and 2016 at 85°W, averaged over 1°S-1°N from the high (black) and low (red) vertical resolution experiments. Dashed curves represent contributions from the convective component.

conducting two model experiments that differ in the vertical discretization, with the resolution in one being significantly higher than in the other in the upper ocean. We find that the difference in the upper-most layer temperature (taken as SST) between the high and low vertical resolution experiments is positive in the equatorial cold tongue and negative along the South American coast, thus reducing the commonly seen cool and warm biases in the two regions, respectively.

In the central equatorial Pacific, going from low to high vertical resolution, the increase in vertical diffusivity, specifically, the increase in the upward gradient of vertical diffusivity in the upper pycnocline, results in a warm anomaly that propagates eastward and rises to the surface to increase SST in the equatorial cold tongue. The change in the structure of the vertical diffusivity, in turn, is the result of an enhancement in the shear-generated turbulence. Power spectra of the vertical shear of the meridional component of velocity at 140°W, equator show a significant increase with increased vertical resolution at wavelengths resolved by both the resolutions (>20 m). Furthermore, the high vertical resolution experiment also captures much of the finer scale vertical velocity shear (<20 m).

The reduction in the cool SST bias in the cold tongue seen in the model experiments highlights the important contribution of fine scale vertical shear to mixing. This result is in line with the observational studies in the western equatorial Pacific, as shown by measurements made with both a high frequency (600 kHz) Acoustic Doppler Current Profiler operated in lowered model (LADCP) and a relatively low frequency (70 kHz) ship-based ADCP (Richards et al., 2012). Vertical shear as measured by the high resolution LADCP is dominated by high peaks at small vertical scales that are not captured by the low resolution ADCP, and these peaks are closely associated with enhanced turbulent kinetic energy dissipation rate estimated using data from a Microstructure Profiler.

In the far eastern equatorial Pacific, the change in vertical diffusivity from low to high vertical resolution in the lower pycnocline produces a cool anomaly that propagates poleward as coastal Kelvin waves along the west coast of the American continent and outcrops along the South American coast to reduce SST there. Stratification appears to be the dominant factor in changing the structure of the vertical diffusivity as seen at 85°W. We hypothesize that the increased vertical resolution helps resolve the fine details of the stratification which is particularly weak beneath the shallow and highly stratified surface layer. By contrast, the low vertical resolution, with 6 layers ranging from 11 to 17 m in thickness in the depth range of 60–140 m (the region

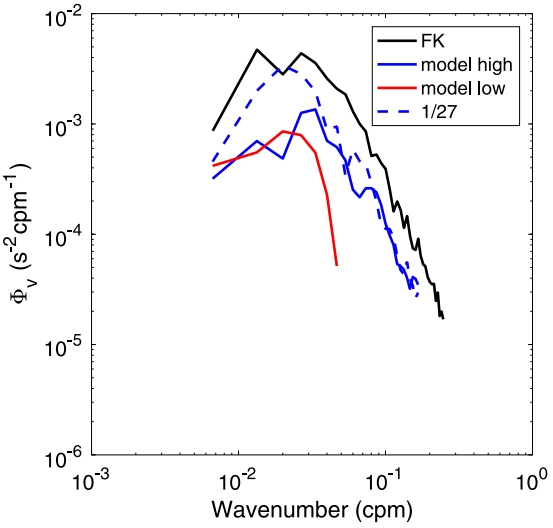

Fig. 13. Φ_v over the depth range of 75–225 m, from R/V Falkor cruise FK150728 (170°W, 1°N, August 2015) and model experiments.

with large changes in vertical diffusivity), is unlikely to represent the weak stratification well.

The impact of subsurface temperature structure in the eastern equatorial Pacific on SST off the South American coast comes as no surprise. Its basis was well laid out in Furue et al. (2015, their Fig. 10). The connection between the two regions is present, though not discussed, in Jia et al. (2015). Our supplementary figure, Fig. S1, is the same as Fig. 13 of Jia et al. (2015) with the eastern limit extended to 70°W. For each case shown in the figure, the temperature anomaly along the equator is shown in Fig. 12 of Jia et al. (2015). Note the aforementioned connectivity, in particular, the contrast between the warm anomaly in the EQWd and EQEd cases versus the cool anomaly in the others. More examples can be seen in Sasaki et al. (2012). In the three experiments shown in Fig. 6a-c of Sasaki et al. (2012), their mixing parameterization results in a positive temperature difference at subsurface of varying magnitude that extends all the way to the eastern boundary. It is by no coincidence that we see warming, including the relative magnitude, off the South American coast in the corresponding experiments in their Fig. 5b-d.

In view of the high connectivity in the tropical Pacific, whether through equatorial Kelvin waves along the equator where SST in the cold tongue can be impacted by mixing in the pycnocline to the west, or through coastal Kelvin waves along the eastern boundary where SST along the South American coast can be impacted by mixing at the equator, high vertical resolution measurements are much needed for an improved knowledge of shear-generated turbulence in the central and eastern regions, and a detailed description of the stratification in the far eastern region.

To illustrate the importance of high vertical resolution, we have conducted model experiments at a relatively coarse horizontal resolution as a compromise between the demand for computation and the need for a basin scale domain. To achieve the observed level of vertical shear, an adequate horizontal resolution is also needed. To demonstrate this point, in Fig. 13, we compare Φ_v from model experiments to data collected using a high resolution (600 kHz) LADCP during a 4-day time series in August 2015 at 170°W, 1°N from R/V Falkor cruise FK150728. The observations show a strongly peaked spectrum, peaking around 50 m wavelength, similar to spectra from measurements in the western equatorial Pacific (see Richards et al., 2015). The shear spectrum from the low vertical resolution experiment falls well below the observations. The high vertical resolution experiment produces a spectrum that fills out much of the higher wavenumbers. There remains, however, a marked deficit for wavelengths greater than 20 m. For comparison we include the shear spectrum from a companion experiment where the model is downscaled in a region surrounding the location of the observations such that the horizontal resolution is 1/27°. With the increased resolution in both the horizontal and vertical directions, the model spectrum is now peaked around 50 m wavelength, approaching that of the observations.

Our results clearly show that adequate vertical resolution is required to capture relatively small vertical scale features in the equatorial ocean and that those features make an important contribution to vertical mixing which in turn impacts the larger scale ocean structure. We suggest that more emphasis is put on resolving these scales in both models and observations and a better understanding is required of their spatial and temporal variability.

Another possible benefit linked to an increase in vertical resolution in models is the likely reduction in numerical diffusion associated with advection schemes. In a study of the formation mechanism of the Pacific equatorial thermocline, Tatebe and Hasumi (2010) showed that by reducing numerical diffusion in a model, SST is increased in the central equatorial Pacific and decreased along the South American coast (their Fig. 9), in much the same way as shown in this study by explicit diffusion. The reduction in numerical diffusion is achieved through the use of a highly accurate advection scheme, the second-order moment (SOM) scheme (Prather, 1986), compared with a third-order scheme that introduces much numerical diffusion. In our model experiments, we use the third-order direct space time (DST) scheme as implemented in MITgcm. Since the same advection scheme is used in our experiments, we may expect some, but limited, cancellation of the effect of numerical diffusion when we compute the difference in potential temperature between experiments. A reduction in numerical diffusion will occur through the increase in vertical resolution, and may have contributed to the changes in SST in addition to the explicit diffusion.

Lastly, we have conducted ocean-only experiments. Coupled experiments are required to quantify the magnitude and temporal variability, which can be done with atmospheric models of varying complexity (see e.g. Zhang et al., 2020). We expect that coupling with the atmosphere will enhance the impact on the cold tongue SST, as shown by Sasaki et al. (2013).

CRediT authorship contribution statement

Yanli Jia: Methodology, Formal analysis, Investigation, Writing - original draft, Writing - reviewing & editing. **Kelvin J. Richards:** Conceptualization, Methodology, Investigation, Writing - reviewing & editing, Supervision, Funding acquisition. **H. Annamalai:** Methodology, Investigation, Writing - reviewing & editing, Funding acquisition.

Declaration of competing interest

The authors declare that they have no known competing financial interests or personal relationships that could have appeared to influence the work reported in this paper.

Acknowledgments

This work was funded by the National Oceanic and Atmospheric Administration (NOAA) [Grant Number NA18OAR4310404], a pre-field modeling study in support of the Tropical Pacific Observing System (TPOS) process studies, a component of TPOS 2020. We thank the support of the Schmidt Ocean Institute and the captain and crew of the R/V Falkor cruise FK150728 in the collection of the LADCP data included in Fig. 13. We appreciate the time and effort of the editors and anonymous reviewers whose comments and suggestions helped improve the manuscript. The authors wish to acknowledge use of the Ferret program for analysis and graphics in this paper. Ferret is a product of NOAA's Pacific Marine Environmental Laboratory. (Information

is available at http://ferret.pmel.noaa.gov/Ferret/). The technical support and advanced computing resources from the University of Hawaii Information Technology Services – Cyberinfrastructure are gratefully acknowledged.

Appendix A. Supplementary data

Supplementary material related to this article can be found online at https://doi.org/10.1016/j.ocemod.2020.101722.

References

Bjerknes, J., 1969. Atmospheric teleconnections from the equatorial Pacific. Mon. Weather Rev. 97, 163–172.

Burls, N.J., Muir, L., Vincent, E.M., Fedorov, A., 2017. Extra-tropical origin of equatorial Pacific cold bias in climate models with links to cloud albedo. Clim. Dyn. 49, 2093–2113. http://dx.doi.org/10.1007/s00382-016-3435-6.

Dee, D.P., Uppala, S.M., Simmons, A.J., Berrisford, P., Poli, P., Kobayashi, S., Andrae, U., Balmaseda, M.A., Balsamo, G., Bauer, P., Bechtold, P., Beljaars, A.C.M., van de Berg, L., Bidlot, J., Bormann, N., Delsol, C., Dragani, R., Fuentes, M., Geer, A.J., Haimberger, L., Healy, S.B., Hersbach, H., Hólm, E.V., Isaksen, L., Kållberg, P., Köhler, M., Matricardi, M., McNally, A.P., Monge-Sanz, B.M., Morcrette, J.-J., Park, B.-K., Peubey, C., de Rosnay, P., Tavolato, C., Thépaut, J.-N., Vitart, F., 2011. The ERA-interim reanalysis: configuration and performance of the data assimilation system. Q. J. R. Meteorol. Soc. 137, 553–597. http://dx.doi.org/10.1002/qj.828.

Furue, R., Jia, Y., McCreary, J.P., Schneider, N., Richards, K.J., Müller, P., Cornuelle, B.D., Martínez Avellaneda, N., Stammer, D., Liu, C., Köhl, A., 2015. Impacts of regional mixing on the temperature structure of the equatorial Pacific Ocean. Part 1: Vertically uniform vertical diffusion. Ocean Model. 91, 91–111. http://dx.doi.org/10.1016/j.ocemod.2014.10.002.

Griffies, S.M., Biastoch, A., Böning, C., Bryan, F., Danabasoglu, G., Chassignet, E.P., England, M.H., Gerdes, R., Haak, H., Hallberg, R.W., Hazeleger, W., Jungclaus, J., Large, W.G., Madec, G., Pirani, A., Samuels, B.L., Scheinert, M., Sen Gupta, A., Severijns, C.A., Simmons, H.L., Treguier, A.M., Winton, M., Yeager, S., Yin, J., 2009. Coordinated ocean-ice reference experiments (COREs). Ocean Model. 26, 1–46. http://dx.doi.org/10.1016/j.ocemod.2008.08.007.

Hu, S., Fedorov, A.V., 2016. Exceptionally strong easterly wind burst stalling El Niño of 2014. Proc. Natl. Acad. Sci. USA 113 (8), 2005–2010. http://dx.doi.org/10.1073/pnas.1514182113.

Jia, Y., Furue, R., McCreary, Jr., J.P., 2015. Impacts of regional mixing on the temperature structure of the equatorial Pacific Ocean. Part 2: Depth-dependent vertical diffusion. Ocean Model. 91, 112–127. http://dx.doi.org/10.1016/j.ocemod.2015.02.007.

Jochum, M., 2009. Impact of latitudinal variations in vertical diffusivity on climate simulations. J. Geophys. Res. 114, C01010. http://dx.doi.org/10.1029/2008JC005030.

Klein, S.A., Hartmann, D.L., 1993. The seasonal cycle of low stratiform clouds. J. Clim. 6, 1587–1606.

Köhl, A., Stammer, D., 2008. Variability of the meridional overturning in the North Atlantic from the 50-year GECCO state estimation. J. Phys. Oceanogr. 38, 1913–1930. http://dx.doi.org/10.1175/2008JPO3775.1.

Köhl, A., Stammer, D., Cornuelle, B., 2007. Interannual to decadal changes in the ECCO global synthesis. J. Phys. Oceanogr. 37, 313–337. http://dx.doi.org/10.1175/JPO3014.1.

Large, W.G., McWilliams, J.C., Doney, S.C., 1994. Oceanic vertical mixing: A review and a model with a nonlocal boundary layer parameterization. Rev. Geophys. 32, 363–403. http://dx.doi.org/10.1029/94RG01872.

Large, W.G., Pond, S., 1981. Open ocean momentum flux measurements in moderate to strong winds. J. Phys. Oceanogr. 11, 324–336.

Large, W.G., Pond, S., 1982. Sensible and latent heat flux measurements over the ocean. J. Phys. Oceanogr. 12, 464–482.

Levine, A.F.Z., McPhaden, M.J., 2016. How the July 2014 easterly wind burst gave the 2015-2016 El Niño a head start. Geophys. Res. Lett. 43, 6503–6510. http://dx.doi.org/10.1002/2016GL069204.

Li, G., Xie, S.-P., 2012. Origins of tropical-wide SST biases in CMIP multi-model ensembles. Geophys. Res. Lett. 39, L22703. http://dx.doi.org/10.1029/2012GL053777.

Li, G., Xie, S.-P., 2014. Tropical biases in CMIP5 multimodel ensemble: the excessive equatorial Pacific cold tongue and double ITCZ problems. J. Clim. 27, 1765–1780. http://dx.doi.org/10.1175/JCLI-D-13-00337.1.

Liu, C., Fang, L., Köhl, A., Liu, Z., Smyth, W.D., Wang, F., 2019a. The subsurface mode tropical instability waves in the equatorial Pacific ocean and their impacts on shear and mixing. Geophys. Res. Lett. 46, 12270–12278. http://dx.doi.org/10.1029/2019GL085123.

Liu, C., Köhl, A., Liu, Z., Wang, F., Stammer, D., 2016. Deep-reaching thermocline mixing in the equatorial Pacific cold tongue. Nature Commun. 7, 11576. http://dx.doi.org/10.1038/ncomms11576.

Liu, C., Wang, X., Köhl, A., Wang, F., Liu, Z., 2019b. The northeast-southwest oscillating equatorial mode of the tropical instability wave and its impact on equatorial mixing. Geophys. Res. Lett. 46, 218–225. http://dx.doi.org/10.1029/2018GL080226.

Liu, C., Wang, X., Liu, Z., Köhl, A., Smyth, W.D., Wang, F., 2020. On the formation of a subsurface weakly sheared laminar layer and an upper thermocline strongly sheared turbulent layer in the eastern equatorial Pacific: interplays of multiple time scale equatorial waves. J. Phys. Oceanogr. 50, 2907–2930. http://dx.doi.org/10.1175/JPO-D-19-0245.1.

Marshall, J., Adcroft, A., Hill, C., Perelman, L., Heisey, C., 1997. A finite-volume, incompressible Navier Stokes model for studies of the ocean on parallel computers. J. Geophys. Res. 102, 5753–5766. http://dx.doi.org/10.1029/96JC02775.

McCreary, J.P., Lu, P., 1994. Interaction between the subtropical and equatorial ocean circulations: the subtropical cell. J. Phys. Oceanogr. 24, 466–497. http://dx.doi.org/10.1175/1520-0485(1994)024<0466:IBTSAE>2.0.CO;2.

Meehl, G.A., Gent, P.R., Arblaster, J.M., Otto-Bliesner, B.L., Brady, E.C., Craig, A., 2001. Factors that affect the amplitude of El Nino in global coupled climate models. Clim. Dyn. 17, 515–526.

Moum, J.N., Perlin, A., Nash, J.D., McPhaden, M.J., 2013. Seasonal sea surface cooling in the equatorial Pacific cold tongue controlled by ocean mixing. Nature 500, 64–67. http://dx.doi.org/10.1038/nature12363.

Natarov, A., Richards, K.J., 2019. Enhanced energy dissipation in the equatorial pycnocline by wind-induced internal wave activity. J. Geophys. Res. Oceans 124, 6200–6217. http://dx.doi.org/10.1029/2019JC015228.

Peters, H., Gregg, M.C., Sanford, T.B., 1991. Equatorial and off-equatorial fine-scale and large-scale shear variability at 140°W. J. Geophys. Res. 96, 16913–16928.

Prather, M.J., 1986. Numerical advection by conservation of second-order moments. J. Geophys. Res. 91, 6671–6681.

Richards, K.J., Kashino, Y., Natarov, A., Firing, E., 2012. Mixing in the western equatorial Pacific and its modulation by ENSO. Geophys. Res. Lett. 39, L02604. http://dx.doi.org/10.1029/2011GL050439.

Richards, K.J., Natarov, A., Firing, E., Kashino, Y., Soares, S.M., Ishizu, M., Carter, G.S., Lee, J.H., Chang, K.I., 2015. Shear-generated turbulence in the equatorial Pacific produced by small vertical scale flow features. J. Geophys. Res. Oceans 120, 3777–3791. http://dx.doi.org/10.1002/2014JC010673.

Richards, K.J., Xie, S.-P., Miyama, T., 2009. Vertical mixing in the ocean and its impact on the coupled ocean-atmosphere system in the eastern tropical Pacific. J. Clim. 22, 3703–3719.

Sasaki, W., Richards, K.J., Luo, J.-J., 2012. Role of vertical mixing Originating from small vertical scale structures above and within the equatorial thermocline in an OGCM. Ocean Model. 57–58, 29–42.

Sasaki, W., Richards, K.J., Luo, J.-J., 2013. Impact of vertical mixing induced by small vertical scale structures above and within the equatorial thermocline on the tropical Pacific in a CGCM. Clim. Dyn. 41, 443–453. http://dx.doi.org/10.1007/s00382-012-1593-8.

Tatebe, H., Hasumi, H., 2010. Formation mechanism of the Pacific equatorial thermocline revealed by a general circulation model with a high accuracy tracer advection scheme. Ocean Model. 35, 245–252. http://dx.doi.org/10.1016/j.ocemod.2010.07.011.

Vannière, B., Guilyardi, E., Toniazzo, T., Madec, G., Woolnough, S., 2014. A systematic approach to identify the sources of tropical SST errors in coupled models using the adjustment of initialized experiments. Clim. Dyn. 43, 2261–2282. http://dx.doi.org/10.1007/s00382-014-2051-6.

Warner, S.J., Moum, J.N., 2019. Feedback of mixing to ENSO phase change. Geophys. Res. Lett. 43, 13920–13927. http://dx.doi.org/10.1029/2019GL085415.

Zhang, R.-H., Gao, C., 2017. Processes involved in the second-year warming of the 2014-15 El Niño event as derived from an intermediate ocean model. Sci. China Earth Sci. 60 (9), 1601–1613.

Zhang, R.-H., Yu, Y., Song, Z., Ren, H.-L., Tang, Y., Qiao, F., Wu, T., Gao, C., Hu, J., Tian, F., Zhu, Y., Chen, L., Liu, H., Lin, P., Wu, F., Wang, L., 2020. A review of progress in coupled ocean-atmosphere model developments for ENSO studies in China. J. Oceanol. Limnol. 38 (4), 930–961. http://dx.doi.org/10.1007/s00343-020-0157-8.

Zhu, Y., Zhang, R.-H., 2018. An argo-derived background diffusivity parameterization for improved ocean simulations in the tropical Pacific. Geophys. Res. Lett. 45, 1509–1517. http://dx.doi.org/10.1002/2017GL076269.

Zhu, Y., Zhang, R.-H., 2019. A modified vertical mixing parameterization for its improved ocean and coupled simulations in the tropical Pacific. J. Phys. Oceanogr. 49, 21–37. http://dx.doi.org/10.1175/JPO-D-18-0100.1.

Zuidema, P., Chang, P., Medeiros, B., Kirtman, B.P., Mechoso, R., Schneider, E.K., Toniazzo, T., Richter, I., Small, R.J., Bellomo, K., Brandt, P., de Szoeke, S., Farrar, J.T., Jung, E., Kato, S., Li, M., Patricola, C., Wang, Z., Wood, R., Xu, Z., 2016. Challenges and prospects for reducing coupled climate model SST biases in the eastern tropical Atlantic and Pacific Oceans: The U.S. CLIVAR eastern tropical oceans synthesis working group. Bull. Am. Meteorol. Soc. 97, 2305–2328. http://dx.doi.org/10.1175/BAMS-D-15-00274.1.